Opto-Electronic Advances

Supplementary information

October 2024, Vol. 7, No. 10

DOI: 10.29026/oea.2024.240085

Cascaded metasurfaces enabling adaptive aberration corrections for focus scanning

Xiaotong Li[1,2†], Xiaodong Cai[1†], Chang Liu[1†], Yeseul Kim[2], Trevon Badloe[3], Huanhuan Liu[4], Junsuk Rho[2,5,6,7] and Shiyi Xiao[1*]

[1]Key Laboratory of Specialty Fiber Optics and Optical Access Networks, Joint International Research Laboratory of Specialty Fiber Optics and Advanced Communication, Shanghai Institute for Advanced Communication and Data Science, Shanghai University, Shanghai 200240, China; [2]Department of Mechanical Engineering, Pohang University of Science and Technology (POSTECH), Pohang 37673, Republic of Korea; [3]Graduate School of Artificial Intelligence, Pohang University of Science and Technology (POSTECH), Pohang 37673, Republic of Korea; [4]Shenzhen Institute of Advanced Technology, Chinese Academy of Sciences, Shenzhen 518055, China; [5]Department of Chemical Engineering, Pohang University of Science and Technology (POSTECH), Pohang 37673, Republic of Korea; [6]Department of Electrical Engineering, Pohang University of Science and Technology (POSTECH), Pohang 37673, Republic of Korea; [7]POSCO-POSTECH-RIST Convergence Research Center for Flat Optics and Metaphotonics, Pohang 37673, Republic of Korea.

[†]These authors contributed equally to this work.

*Correspondence: Shiyi Xiao, E-mail: phxiao@shu.edu.cn

This file includes:

Supplementary information for this paper is available at https://doi.org/10.29026/oea.2024.240085

Section 1: Derivation of Eq. (1)

The target phase profile is expressed as

$$\Phi_{\text{target}}(\boldsymbol{r},t)=-k_0\left(\sqrt{(x-x_c(t))^2+(y-y_c(t))^2+z_c^2(t)}-\sqrt{x_c^2(t)+y_c^2(t)+z_c^2(t)}\right)\ , \tag{S1}$$

where k_0 and $\boldsymbol{r}$ are defined in Eq. (1) in the main text. Based on paraxial approximation, Eq. (S1) can be expressed as:

$$\Phi_{\text{target}}(\boldsymbol{r},t)\approx -k_0\frac{x^2+y^2-2xx_c(t)-2yy_c(t)}{2\sqrt{x_c^2(t)+y_c^2(t)+z_c^2(t)}}\ . \tag{S2}$$

By doing some basic algebra, it can be further rewritten as (under paraxial approximation):

$$\Phi_{\text{target}}(\boldsymbol{r},t)\approx \Phi^{\text{moiré}}+\Phi^{\text{grad}}+\Phi^{\text{lens}}\ , \tag{S3}$$

where $\Phi^{\text{lens}}=-k_0(\sqrt{x^2+y^2+F_0^2}-F_0)$, $\Phi^{\text{grad}}=k_0(xx_c(t)+yy_c(t))\Big/\sqrt{x_c^2(t)+y_c^2(t)+z_c^2(t)}$, and $\Phi^{\text{moiré}}=-k_0(x^2+y^2)(F_0-\sqrt{x_c^2(t)+y_c^2(t)+z_c^2(t)})\Big/2F_0\sqrt{x_c^2(t)+y_c^2(t)+z_c^2(t)}$. By considering the three phase functions $\Phi_i^{\text{lens}}(\boldsymbol{r}_i)$, $\Phi_i^{\text{moiré}}(\boldsymbol{r}_i)$, $\Phi_i^{\text{grad}}(\boldsymbol{r}_i)$ for each metasurface layer, the Eq. (S3) can be finally rewritten as a linear combination of the following three terms:

$$\Phi_{\text{target}}(\boldsymbol{r},t)\approx \sum\nolimits_i\Phi_i^{\text{lens}}(\boldsymbol{r}_i)+\sum\nolimits_i\Phi_i^{\text{moiré}}(\boldsymbol{r}_i)+\sum\nolimits_i\Phi_i^{\text{grad}}(\boldsymbol{r}_i)\ , \tag{S4}$$

where $\Phi_i^{\text{moiré}}(r_i)=(-1)^{i-1}\chi_0(u_i^2+v_i^2)\text{mod}\left(\arg(u_i+\text{i}v_i)+\phi_i+\pi\right)$, $\Phi_i^{\text{grad}}(\boldsymbol{r}_i)=\zeta_i v_i$, and $\Phi_i^{\text{lens}}(\boldsymbol{r}_i)=-k_0(\sqrt{u_i^2+v_i^2+F_0^2}-F_0^2)/2$. Hence, Eq. (2) in the main text can be obtained.

Section 2: The longitudinal displacement of focal spot in hyperbolic scanning lenses during scanning process

As shown in Fig. S1, when the focal spot scans in the *xz*-plane, the distance between the focal position and the center of the meta-device is constant and will not change with the scanning angle. Here, z_c represents the distance between the focus and the center of the meta-device, and Δz_c represents the longitudinal displacement of the focal spot during scanning. Since the distance between the focal spot and the center of the metasurface is always equal to z_c, the focal position can be expressed as $(z_c\sin(\Delta\alpha), 0, z_c\cos(\Delta\alpha))$ during scanning process and the longitudinal displacement of the focal spot (Δz_c) can be expressed as:

$$\Delta z_c=z_c\left(1-\cos(\Delta\alpha)\right)\ . \tag{S5}$$

Therefore, the longitudinal focal position decreases as the scanning angle increases, resulting the focal spot deviating

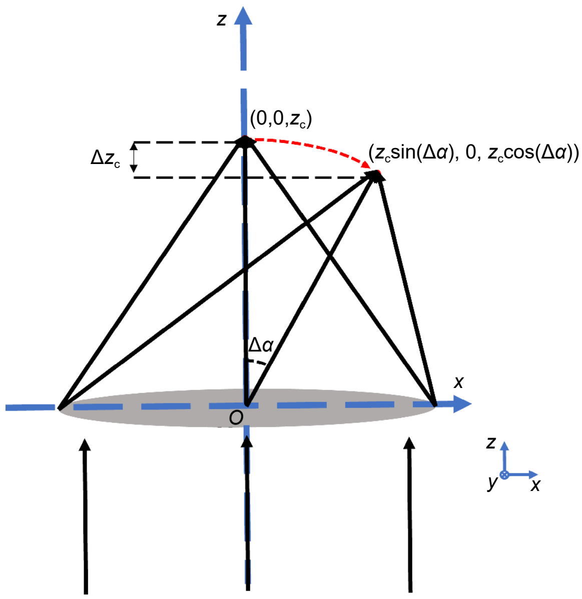

Fig. S1 | Schematic of the focus scanning in the *xz*-plane.

from the target scanning surface.

For instance, when the target scanning surface is a plane ($z_c = 4$ mm), the longitudinal focal positions are $z_c = 4$ mm and $z_c = 3.06$ mm for different scanning angles ($\alpha_2 = -\alpha_1 = 0°$, $\alpha_2 = -\alpha_1 = 40°$) respectively and the longitudinal displacement is $\Delta z_c = 0.94$ mm. Table S1 shows the theoretical focus position and the longitudinal displacement changes with the scanning angle $\Delta\alpha$ when the target scanning surface is $z_c = 4$ mm plane.

Table S1 | The theoretical focus position and the longitudinal displacement changes with the scanning angle $\Delta\alpha$.

Scanning angle (°)	Longitudinal focal position (mm)	Longitudinal displacement (mm)
0	4	0
5	3.98	0.02
10	3.94	0.06
15	3.86	0.14
20	3.76	0.24
25	3.62	0.38
30	3.46	0.54
35	3.28	0.72
40	3.06	0.94
45	2.8	1.2
50	2.57	1.43

Section 3: Quadratic phase reinterpretation of cascaded moiré phase function

The cascaded moiré phase function of our proposed meta-device can be regarded as a special quadratic phase with the focal length varying with the rotation angle α_i (i=1, 2). Based on the S1 in Supplemental information, we have already obtained the phase distribution of the i'th layer as shown in the main text, which is composed of three phase functions ($\Phi_i^{\text{lens}}(\boldsymbol{r}_i)$, $\Phi_i^{\text{grad}}(\boldsymbol{r}_i)$, and $\Phi_i^{\text{moiré}}(\boldsymbol{r}_i)$). For the cascaded moiré phase function, as the rotation operation is periodic, we only need to consider the change of the combined moiré phase $\sum_i \Phi_i^{\text{moiré}}(\boldsymbol{r}_i)$ within the rotation angle of $\alpha_2 - \alpha_1 + \phi_2 - \phi_1 \in (-2\pi, 2\pi]$, which can be expressed as:

For $\alpha_2 - \alpha_1 + \varphi_2 - \varphi_1 \in (-2\pi, 0]$,

$$\sum_i \Phi_i^{\text{moiré}}(\boldsymbol{r}_i) = \begin{cases} \chi_0 r^2(\alpha_2 - \alpha_1 + \varphi_2 - \varphi_1) & 0 < \beta \leqslant \alpha_2 + \varphi_2 + \pi,\ \alpha_1 + \varphi_1 + \pi < \beta \leqslant 2\pi \\ \chi_0 r^2(\alpha_2 - \alpha_1 + \varphi_2 - \varphi_1 + 2\pi) & \alpha_2 + \varphi_2 + \pi < \beta \leqslant \alpha_1 + \varphi_1 + \pi \end{cases}, \tag{S6}$$

where $r = \sqrt{x^2 + y^2}$ and β is the polar angle.

For $\alpha_2 - \alpha_1 + \varphi_2 - \varphi_1 \in (0, 2\pi]$

$$\sum_i \Phi_i^{\text{moiré}}(\boldsymbol{r}_i) = \begin{cases} \chi_0 r^2(\alpha_2 - \alpha_1 + \varphi_2 - \varphi_1) & 0 < \beta \leqslant \alpha_1 + \varphi_1 + \pi,\ \alpha_2 + \varphi_2 + \pi < \beta \leqslant 2\pi \\ \chi_0 r^2(\alpha_2 - \alpha_1 + \varphi_2 - \varphi_1 - 2\pi) & \alpha_1 + \varphi_1 + \pi < \beta \leqslant \alpha_2 + \varphi_2 + \pi \end{cases}, \tag{S7}$$

here, we choose $\alpha_2 - \alpha_1 + \varphi_2 - \varphi_1 \in (-2\pi, 0]$ and Region I as working area in our design, as shown in main text.

On the other hand, the quadratic phase profile is expressed as:

$$\Phi^{\text{quad}}(\boldsymbol{r}) = -\frac{k_0 r^2}{2F}, \tag{S8}$$

where F is the focal length of quadratic phase. By calculating Eq. (S6) and (S8), we find the cascaded moiré phase function can be regarded a special quadratic phase with a variable focal length controlled by the rotation angle, which can be expressed as:

$$F = \begin{cases} \dfrac{k_0}{2\chi_0(\alpha_2 - \alpha_1 + \varphi_2 - \varphi_1)} & 0 < \beta \leqslant \alpha_2 + \varphi_2 + \pi,\ \alpha_1 + \varphi_1 + \pi < \beta \leqslant 2\pi \\ \dfrac{k_0}{2\chi_0(\alpha_2 - \alpha_1 + \varphi_2 - \varphi_1 + 2\pi)} & \alpha_2 + \varphi_2 + \pi < \beta \leqslant \alpha_1 + \varphi_1 + \pi \end{cases}. \tag{S9}$$

Hence, Eq. (S9) indicates that the cascaded moiré phase function consists of two regions, both capable of focusing, and their area ratio and focal length vary with the changing of rotation angle.

Section 4: Meta-atom design

We now employ the proposed strategy to realize self-corrected varifocal metalens in the THz regime, starting from the meta-atom designs. To ensure high transmittance of the meta-device, we choose all-dielectric materials (silicon) to design the meta-atom. Figure S2(a) schematically shows the geometry of a typical meta-atom, which consists of two silicon posts deposited on the different sides of a continuous silicon spacer. Both square silicon pillars, positioned at the top and bottom, exhibit isotropic properties to achieve polarization insensitivity. The bottom silicon post primarily serves to minimize the reflection of THz waves to enhance transmittance. The desired phase ($0-2\pi$) is achieved by varying the side length (w_1) of the top silicon post. The total height of the meta-atom is 500 μm ($h_1+h_2+h_3$), which corresponds to the standard thickness of silicon, to facilitate subsequent sample manufacturing.

We first present the design approach for the top silicon post. For normally incident THz waves, we investigate how the transmission characteristics and phase of meta-atoms without the bottom silicon post vary against two geometric parameters of w_1 and h_1, while keeping other parameters fixed at $h_2 = 140$ μm, $P = 140$ μm. Figure S2(b) illustrates the transmission coefficient and phase computed by finite-difference time-domain (FDTD) simulations at 0.6 THz, as varying w_1 and h_1. Clearly, within the range of geometric parameter variations for the top silicon post, meta-atoms consistently achieve high transmission and $0-2\pi$ phase coverage. Finally, we determine the height of the top silicon post as $h_1 = 300$ μm.

Then we show how to design the bottom silicon post. Figure S2(c) shows the transmittance and phase of meta-atoms varying against w_1 and w_3. We find that the transmittance of the meta-atoms can be effectively increased by adding the l bottom silicon post while ensuring the $0-2\pi$ phase coverage. Finally, we determine the side length of square cross-section of the bottom silicon post as $w_3 = 70$ μm and achieve the required phase by varying the side length of square cross-section of the top silicon post. Therefore, the optimal parameters of meta-atom are $h_1 = 300$ μm, $h_2 = 140$ μm, $h_3 = 60$ μm, $P = 140$ μm, $w_3 = 70$ μm.

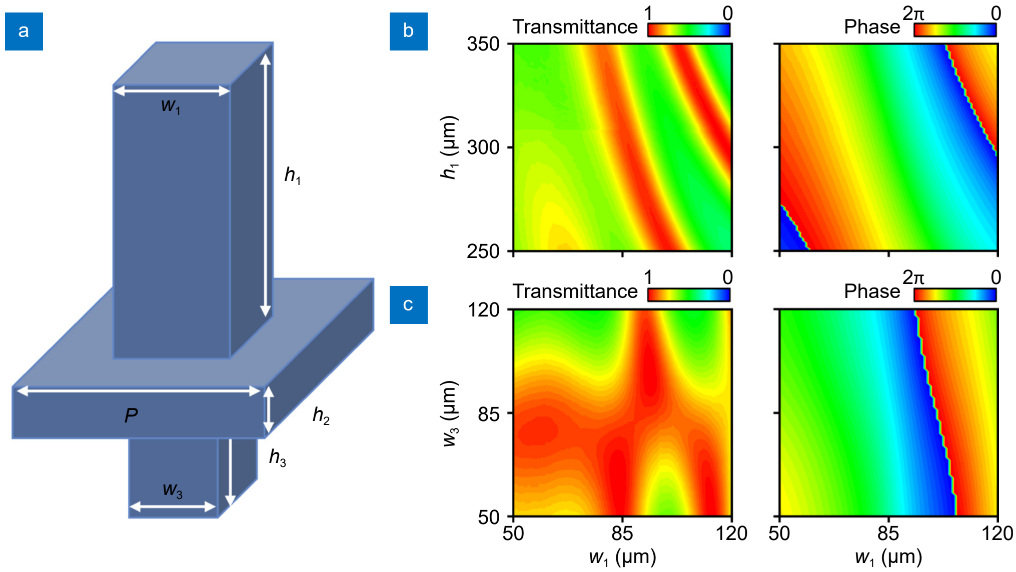

Fig. S2 | Meta-atom design. (**a**) Schematic of meta-atom. (**b**) The transmission coefficient and phase of meta-atom without the bottom silicon post. (**c**) The transmission coefficient and phase of meta-atom.

Section 5: Optimization of the spacing distance between layers

We demonstrate the performance of our proposed meta-device (the first device studied in the main text) at different spacing distances to choose the optimial spacing distance between layers. As shown in Fig. S3, the performance decays as the spacing distance increases, and the meta-device with a spacing distance of 100 μm has the best scanning aberration correction ability. However, such a small gap (100 μm) is very hard to be realized in experiments. In our case, we finally set the spacing distance as 300 μm to compromise the device's performance and the practical realization in experiments.

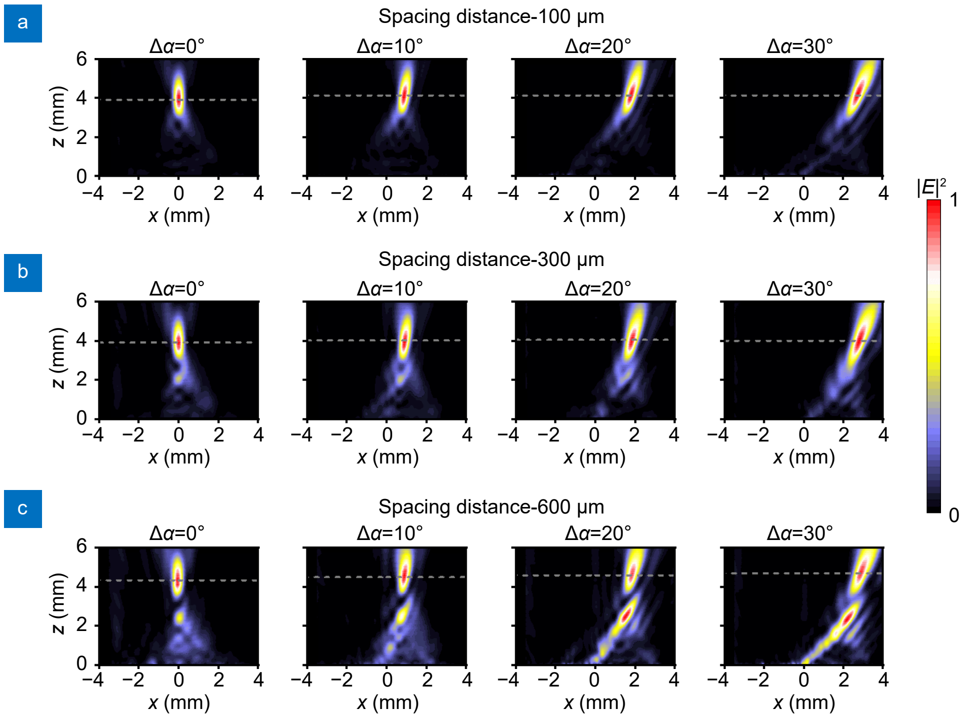

Fig. S3 | The simulated result of meta-device for adaptively corrected planar scanning at different Δα corresponding to different spacing distance. (**a**) 100 μm, (**b**) 300 μm, and (**c**) 600 μm.

Section 6: Fabrication of samples and experimental setup

As mentioned in the previous section, the sample fabrication involved deep silicon etching on both sides of a double-sided polished high-resistivity intrinsic silicon wafer as per the following, as shown in Fig. S4.

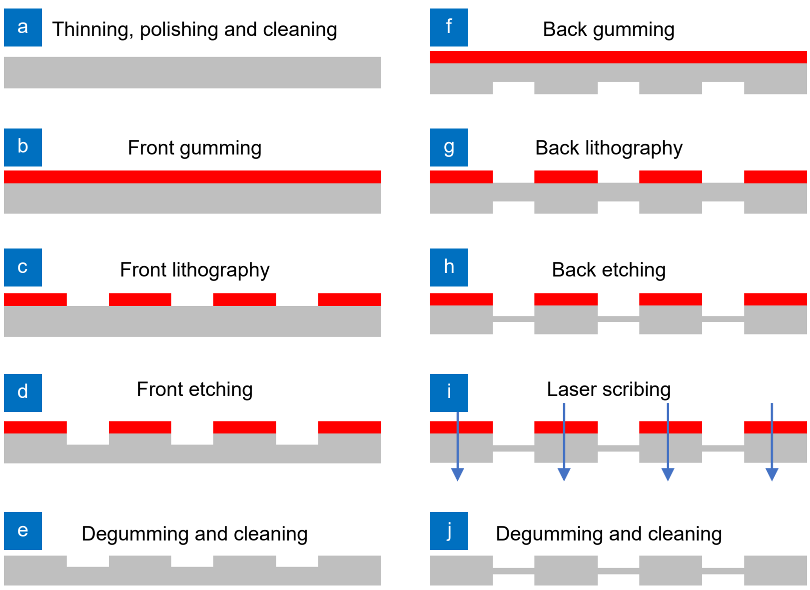

Fig. S4 | (**a**–**j**) Process of sample fabrication.

(1) Substrate preparation: A silicon substrate with a thickness of 500 μm was selected and subjected to a series of cleaning steps to remove organic and inorganic contaminants from the surface. Finally, the substrate was baked at a high temperature to eliminate surface moisture.

(2) Bottom coating: Apply a layer of bottom photoresist and the comparison of different photoresists is shown in Table S2. Photoresist is an organic compound that changes its solubility in a developer after being exposed to ultraviolet light. Photoresist is applied directly to the surface of the substrate material in liquid form and then dried into a film. There are two types of photoresists: negative photoresist, which hardens after being exposed to ultraviolet light and cannot be dissolved in a developer. Positive photoresist, in which the exposed part softens and can be dissolved by a developer. The substrate easily absorbs moisture in the air to its surface, but the substrate surface needs to be kept dry when applying photoresist. We need to perform surface treatment on the substrate to improve the adhesion between the photoresist and the substrate so that the photoresist will not be penetrated by the developer during the development process and control the thickness of the photoresist to meet design specifications.

(3) Bottom lithography: Use ultraviolet light to expose the bottom photoresist through a mask, defining the desired pattern. Use an ultraviolet lithography machine to expose the photoresist through the mask. During exposure, the lithography machine will align the marks on the substrate to ensure the precise position of the pattern. During exposure, the photoacid generator (PAG) in the photoresist decomposes to produce acid, which will trigger a chemical reaction in the subsequent steps. After exposure, the substrate is usually post-exposure baked at a higher temperature (about 110–130 °C) to allow the acid in the photoresist to diffuse and induce backbone cleavage or cross-linking reactions to form soluble or insoluble areas.

(4) Bottom development: Develop the bottom photoresist to remove unexposed areas, exposing the silicon substrate. This step forms the bottom lithography pattern. The substrate is immersed in a developer (usually an alkaline solution), which dissolves the photoresist in the exposed or unexposed areas (depending on the type of photoresist, positive or negative), thus forming the desired pattern. The developed substrate is baked at a higher temperature (about 150–180 °C) to further cure the photoresist and improve the etch resistance.

(5) Dielectric layer Deposition: Deposit a dielectric layer, such as silicon dioxide or silicon nitride, onto the bottom lithography pattern. This layer serves as an insulator.

(6) Top coating: Apply a layer of top photoresist, also a UV-sensitive polymer, onto the dielectric layer.

(7) Top lithography: Use a UV light source through a different mask to expose the top photoresist, defining the final device shape.

(8) Top development: Develop the top photoresist to remove unexposed areas, exposing the dielectric layer or the bottom lithography pattern. This step forms the top lithography pattern.

(9) Etching: Employ etching techniques. We use NAURA HSE200 etching machine, etched gas is C4F8/SF6 with C4F8:SF6=5:2 in 10 mTorr pressure to remove the exposed dielectric layer and silicon substrate, forming the ultimate micro/nanostructures.

(10) Cleaning and inspection: Clean the sample to remove residual photoresist and impurities. After a series of operations, the photoresist loses its function, and we remove the glue layer. There are two methods for removing the glue: wet method and dry method. The wet method is to use various inorganic solvents or organic solvents to etch away the glue layer. The most used solvent is acetone, which can dissolve a variety of photoresists. The dry method is to use oxygen plasma etching to remove the glue, but it is not suitable for all samples and needs to be considered according to the actual situation. Finally, inspect the sample using tools like a microscope to ensure the desired patterns and structures have been achieved.

These procedures may undergo variations depending on specific processes and equipment; nevertheless, in essence,

Table S2 | The parameters of SU-8 photoresist with different thickness.

Thickness (um)	Glue shedding rate (rpm)		Pre-baking time (min)		Post-baking time (min)	Post-baking time (min)	
	Pre-homogenization	High-speed homogenization	65 °C	95 °C	65 °C	95 °C	
34.61	400	4000	10	20	30	5	4
73.65	400	2000	20	30	30	10	8
237.83	300	800	30	90	30	20	14

photolithography is a photochemical-based technique employed to generate the desired patterns on the surface.

The etching variations are inevitably present, such as: the variations in etching depths at different positions on the same etched surface; non-vertical etching results in disparate sizes of the upper and lower cross-sections of the etched silicon pillars, and so on. Therefore, it is necessary to apply compensations to the cross-sectional width of the top silicon post of the meta-atom on the drawings. This is done to mitigate etching variations and achieve our anticipated functionality. The final cross-sectional widths of the top silicon posts of metasurfaces are depicted in the Fig. S5.

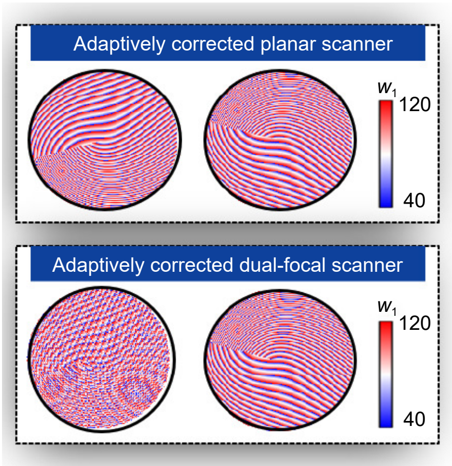

Fig. S5 | The cross-sectional width of the top silicon posts at different positions on the samples.

We measured the performance of the designed meta-device using a terahertz time-domain spectroscopy (THz-TDS) system. The system uses advanced scanning technology. The terahertz electric field information is received by a probe located above the samples and the probe can move with high precision within a range of 10 × 10 mm to ensure comprehensive acquisition and accurate recording of the signal. As shown in Fig. S6(a), the linearly polarized terahertz wave emitted from the emitter is converted into a plane wave by the lens firstly, and then passing through two layers of cascaded metasurfaces. Finally, the information of THz wave is collected by the linearly polarized receiver which is fixed above the sample. As shown in Fig. S6(b), we fixed the cascaded metasurfaces to a specific sample stage and controlled the rotation of the sample stage by a servomotor during the experiment. The rotary table is driven by piezoelectric resonant motor technology and is removable between the rotary tables to ensure that samples can be mounted. A removable sample mounting base plate is attached to the round hole of the rotary table to accommodate samples of different sizes. The rotary table consists of the following operating modes: continuous rotation, co-rotation, counter-rotation, rotation to a fixed angle and hold. The mount's swivel groove is internally threaded and contains two retaining rings for mounting the optics. The mount is lightweight and compact and can be rotated in the desired direction in closed-loop operation. The motor is powerful and gearless, with the stroke is 360° and the accuracy is 0.05°.

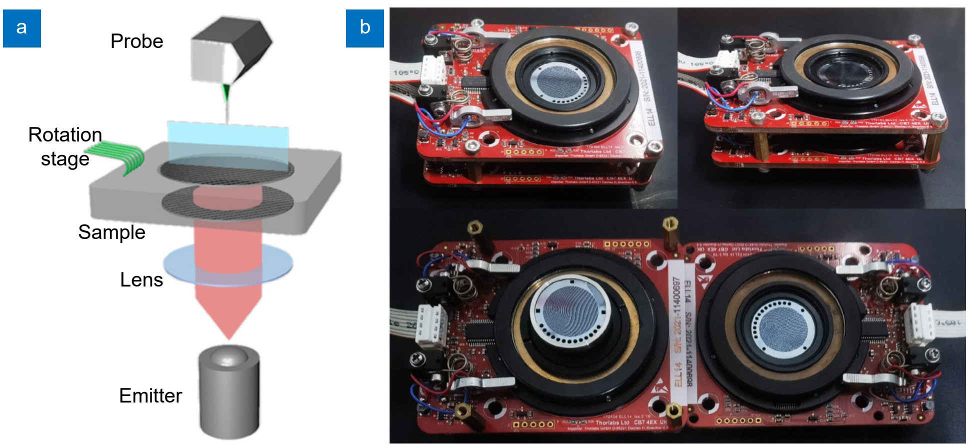

Fig. S6 | The experimental setup. (**a**) Near-field measurement platform. (**b**) The motorized rotation stage and samples.

Section 7: The proposed meta-device compared to hyperbolic scanning lenses and quadratic scanning lenses

7.1 The result of hyperbolic scanning lenses

Hyperbolic scanning lenses is denoted as a type of scanning lens with phase distribution which can be expressed as

$$\Phi_i(\boldsymbol{r}_i) = \Phi_i^{\text{lens}}(\mathbf{r}_i) + \Phi_i^{\text{grad}}(\boldsymbol{r}_i) \ , \tag{S10}$$

where $\Phi_i^{\text{lens}}(\boldsymbol{r}_i)$ and $\Phi_i^{\text{grad}}(\boldsymbol{r}_i)$ are defined in the main text and we choose $F_0 = 8\lambda$ in this case. As shown in Fig. S7, the

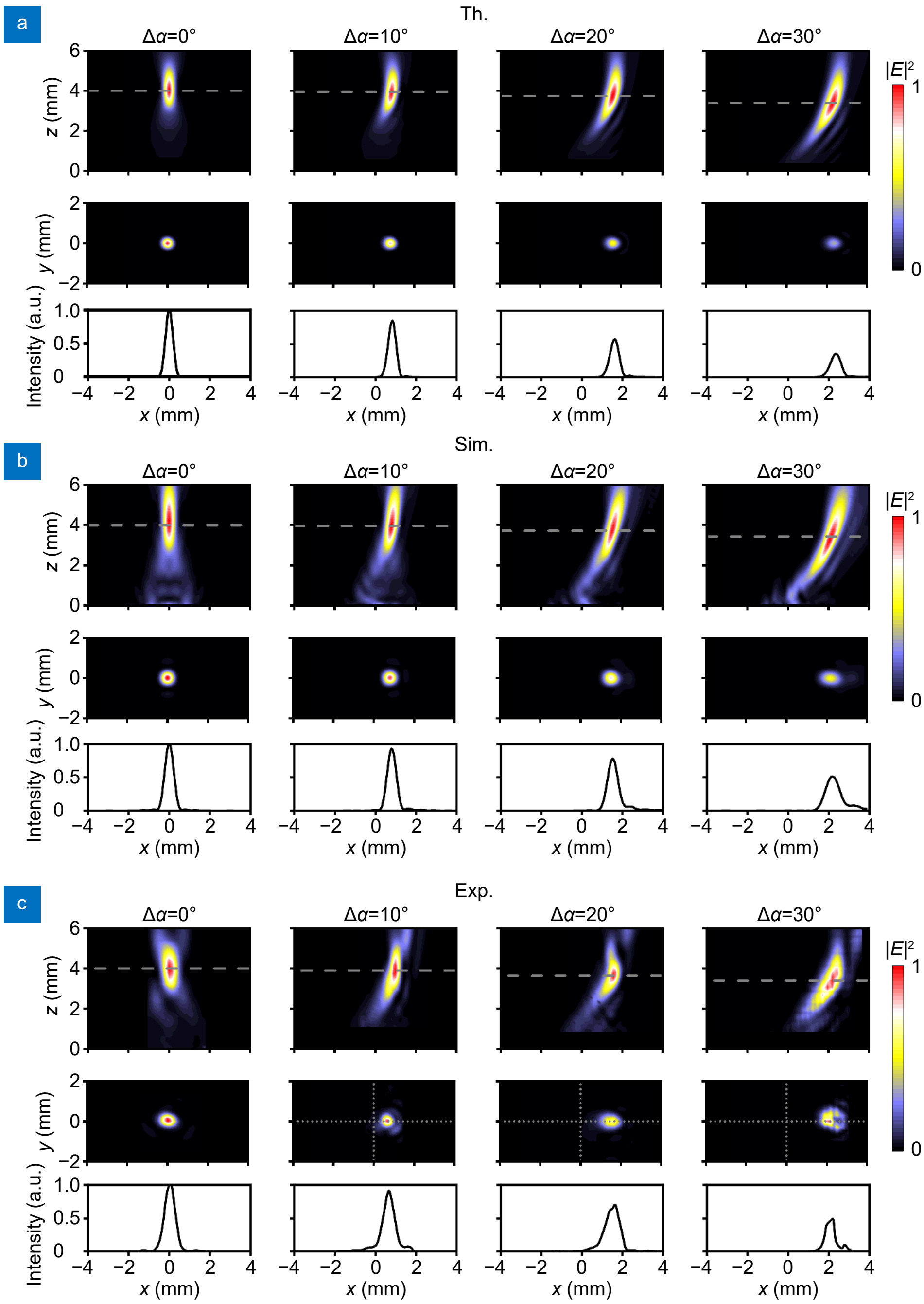

Fig. S7 | Terahertz characteristics of the hyperbolic scanning lenses for planar scanning. (**a**) Theoretical, (**c**) experimental and (**d**) simulated intensity distributions on *xz*-plane (top) and *xy*-plane (middle) corresponding to different Δ*α* and the intensity profiles along the diameter (bottom) at the focal plane with the full width at half maximum (FWHM) marked. Here, the grey dashed line in (a), (b) and (c) represents the position of the maximum intensity of focal spot.

longitudinal position of the focal point decreases with the lateral position of the focal point increasing, resulting in the scanning surface is curved $z_c = F_0\cos(\Delta\alpha)$. The theoretical, simulated, and experimental intensity distributions are in good agreement. The scanning aberration (defined in the main text) of hyperbolic scanning lenses is around 6.56% on average (15% at the maximum scanning angle) within the scanning range of ±30°.

7.2 The result of quadratic scanning lenses

Quadratic scanning lenses is denoted as a type of scanning lens with the phase distribution of quadratic phase profile as

$$\begin{cases} \Phi_1(\boldsymbol{r}_1) = \Phi^{\text{quad}}(\boldsymbol{r}_1) + \Phi_1^{\text{grad}}(\boldsymbol{r}_1) \\ \Phi_2(\boldsymbol{r}_2) = \Phi_2^{\text{grad}}(\boldsymbol{r}_2) \end{cases}, \tag{S11}$$

where $\Phi^{\text{quad}}(\boldsymbol{r}_1)$ and $\Phi_i^{\text{grad}}(\boldsymbol{r}_i)$ are defined in Eq. (S8) and main text, respectively. In this case we choose $F = 8\lambda$. As shown in Fig. S8, the longitudinal position of focal point basically unchanged and the average scanning aberration is around 3.9% within the scanning range of ±30°. The theoretical and simulated intensity distribution are in good agreement.

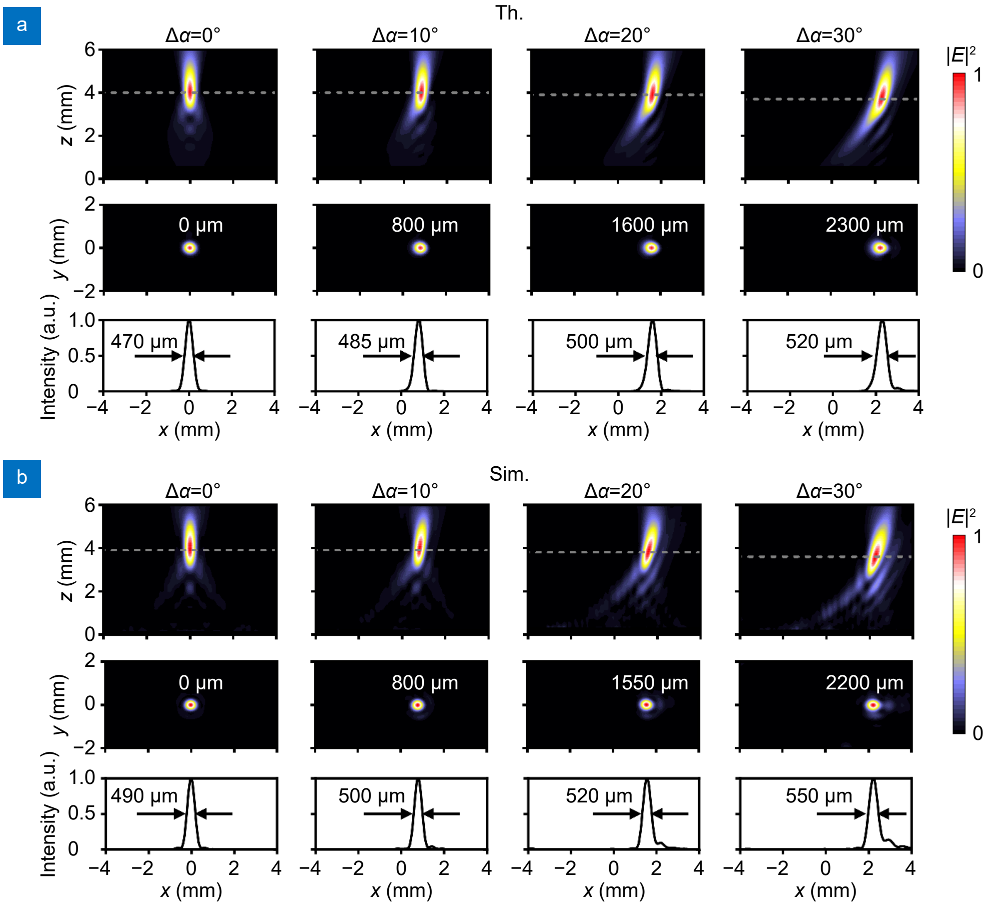

Fig. S8 | Terahertz characteristics of quadratic scanning lenses for planar scanning. (**a**) Theoretical, and (**b**) simulated intensity distributions on *xz*-plane (top) and *xy*-plane (middle) corresponding to different Δ*α*, and the intensity profiles along the diameter (bottom) at the focal plane with the FWHM marked. Here, the grey dashed line in (a) and (b) represents the position of the maximum intensity of focal spot.

7.3 Comparison between different mate-devices

We compare our proposed meta-device with other scanning systems (hyperbolic scanning lenses and quadratic scanning lenses) to demonstrate the advantages in scanning aberration correction. The results of different target scanning surfaces (planar surface and conical surface) are shown in Tables S3–S6.

Table S3 | Comparison of scanning aberration of meta-devices for planar scanning.

Comparison of scanning aberration of different meta-devices for planar scanning						
Meta-devices	Theory		Simulation		Experiment	
	At maximum scanning angle ± 30°	Within the scanning range of [−30°, 30°]	At maximum scanning angle ± 30°	Within the scanning range of [−30°, 30°]	At maximum scanning angle ± 30°	Within the scanning range of [−30°, 30°]
Hyperbolic scanning lenses	15	5.82	15	6.06	15.5	6.56
Quadratic scanning lenses	7.5	2.5	10	3.9	-	-
Our proposed meta-device	1.25	0.94	0.5	1	1.5	1.18

Table S4 | Experimental comparison of the focal quality of meta-devices for planar scanning.

Experimental comparison of the focal quality of different meta-devices for planar scanning		
Meta-devices	Focal shape at maximum scanning angle ±30°	Focal intensity within the scanning range of [−30°, 30°]
Hyperbolic scanning lenses	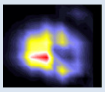	0.62
Quadratic scanning lenses	-	-
Our proposed meta-device	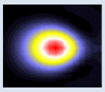	0.73

Table S5 | Comparison of scanning aberration of meta-devices for conical scanning.

Comparison of scanning aberration of different meta-devices for conical scanning						
Meta-devices	Theory		Simulation		Experiment	
	At maximum scanning angle ±30°	Within the scanning range of [−30°, 30°]	At maximum scanning angle ±30°	Within the scanning range of [−30°, 30°]	At maximum scanning angle ±30°	Within the scanning range of [−30°, 30°]
Hyperbolic scanning lenses	14	5.25	14	5.5	14	5.8
Quadratic scanning lenses	14	6.8	14	7	-	-
Our proposed meta-device	5	3.8	4	4.4	8.3	4.6

Table S6 | Experimental comparison of the focal quality of meta-devices for conical scanning.

Experimental comparison of the focal quality of different meta-devices for conical scanning		
Meta-devices	Focal shape at maximum scanning angle ±30°	Focal intensity within the scanning range of [-30°, 30°]
Hyperbolic scanning lenses		0.6
Quadratic scanning lenses	-	-
Our proposed meta-device		0.68

When the target scanning surface is planar, the experimental result demonstrates that our proposed meta-device dynamically scans the focal spot on the target surface, achieving the average scanning aberration of 1.18% and average intensity of 0.73 within the scanning range of ±30°. Compared with hyperbolic scanning lenses, our proposed meta-device reduces the average scanning aberration by a factor 5.56 (from 6.56% to 1.18%) and enhances the average intensity by a factor 1.18 (from 0.62 to 0.73). Similarly, we note quadratic scanning lenses suitably correct scanning aberrations, which can reduce the average scanning aberration by a factor 1.55 (from 6.06% to 3.9%) compared to the hyperbolic scanning lenses as shown in the simulation.

When the target scanning surface is conical, the experimental result demonstrates that our proposed meta-device dynamically scans the focal spot on the target surface, achieving the average scanning aberration of 4.6% and average intensity of 0.68 within the scanning range of ±30°. Compared with hyperbolic scanning lenses, our proposed meta-device can effectively reduce the average scanning aberration by a factor 1.26 (from 5.8% to 4.6%) and enhance the average intensity by a factor 1.13 (from 0.60 to 0.68). However, quadratic scanning lenses cannot reduce the displacement between the focal position and the target conical surface, indicating that it can only achieve scanning aberration correction in planar scanning.

Section 8: The demonstration of customized scanning trajectory

To demonstrate our proposed meta-device has ability to scan different trajectories, we conducted experiments to demonstrate the S-shaped scanning trajectory of the focal spot on $z = 4$ mm plane, as shown in Fig. S9. The target scanning trajectory which can be expressed as:

$$y_c(t) = \cos\left(\frac{3\pi}{4}x_c(t)\right) \text{ for } -2 \le x_c(t) \le 2\,, \tag{S12}$$

where $x_c(t)$ and $y_c(t)$ represent the position of the focal spot and the arrow indicates the moving direction. Based on the Eq. (4) in the main text, we can obtain the relationship between the target scanning trajectory and the rotation angle of cascaded metasurfaces as:

$$\begin{cases} \sqrt{\cos^2\left(\frac{3\pi}{4}x_c(\Delta\alpha, \alpha_{av})\right) + x_c^2(\Delta\alpha, \alpha_{av})} = \sin(\Delta\alpha)R_c(F_0, x_0, \varphi_0, \Delta\alpha) \\ \arg\left(x_c(\Delta\alpha, \alpha_{av}) + \mathrm{j}\cos\left(\frac{3\pi}{4}x_c(\Delta\alpha, \alpha_{av})\right)\right) = \alpha_{av} \end{cases}, \tag{S13}$$

where $\Delta\alpha$, α_{av}, and $R_c(F_0, \chi_0, \phi_0, \Delta\alpha)$ are defined in the main text and the arg function is used to calculate the main argument of the complex number. By calculation, the rotation angle of the metasurfaces corresponding to the scanning trajectory is shown in Fig. S9(b). The experimental intensity distributions of focal spot on the $z = 4$ mm plane by elec-

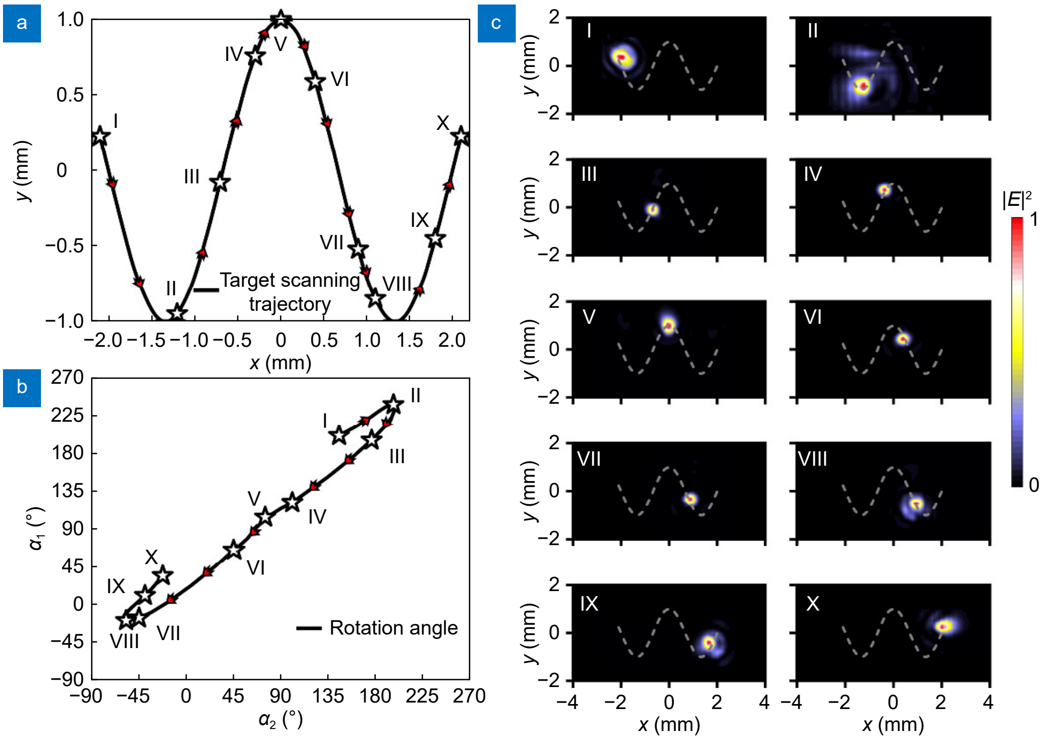

Fig. S9 | The demonstration of S-shaped scanning trajectory of adaptively corrected planar scanner. (**a**) The target scanning trajectory of the adaptively corrected planar scanner and the arrows represent the movement of focal position during scanning. (**b**) The rotation angle of the metasurface during scanning. The arrows represent the movement of focal position during scanning. (**c**) Experimental intensity distributions of focal spot on the z = 4 mm plane during scanning. The dashed line presents the target scanning trajectory.

trically controlling the motorized rotation stage via program are shown in Fig. S9(c) and the dashed line presents the target scanning trajectory. Table S7 shows the different target focal positions and the corresponding rotation angles of metasurfaces, as well as the position of the maximum field intensity on the z = 4 mm plane in experiment. The theoretical and experimental result are in good agreement.

Table S7 | The rotation angle and the focal position correspond to the target scanning trajectory during the experiment.

Focal spot	Target scanning trajectory (mm)		Rotation angle (°)		Experimental focal position (mm)	
Number	X	y	a_1	a_2	X	y
I	−2.1	0.23	145	200	−2	0.4
II	−1.2	−0.95	200	240	−1.2	−0.8
III	−0.7	−0.08	180	200	−0.75	−0.1
IV	−0.3	0.76	100	125	−0.35	0.7
V	0	1	75	105	0	1
VI	0.4	0.59	45	65	0.4	0.4
VII	0.9	−0.52	−45	−15	0.9	−0.3
VIII	1.1	−0.85	−55	−20	1	−0.6
IX	1.8	−0.45	−40	10	1.7	−0.4
X	2.1	0.23	−20	35	2	0.2

Section 9: Experimental results of *y*-polarized incidence

To demonstrate our proposed meta-device can work under y-polarized THz wave incidence. We conduct experiments of y-polarized THz wave incidence. As shown in Fig. S10, the lateral position of focal point moved with the metasurface rotating and the longitudinal position of focal point basically unchanged. The experimental result is consistent with result of x-polarized THz wave incidence, demonstrate the polarization insensitivity of our proposed meta-device.

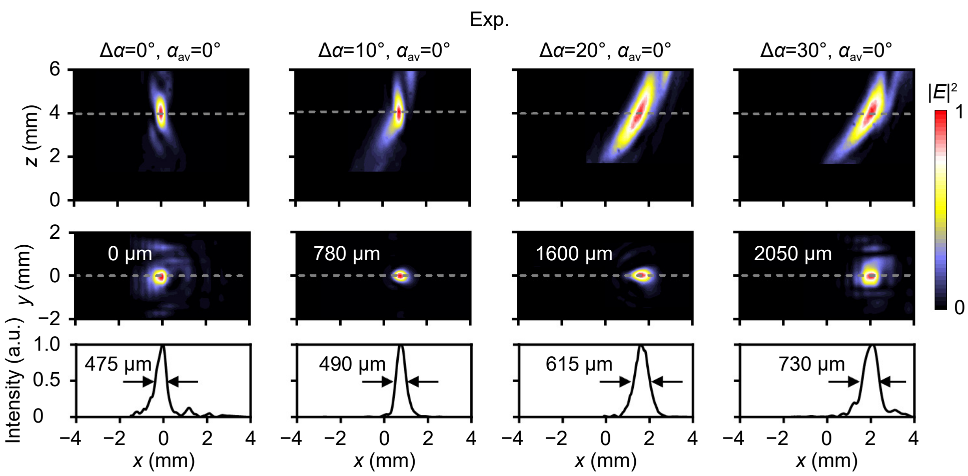

Fig. S10 | The experimental results of the meta-device for adaptively corrected planar scanning with *y*-polarization incident.

Section 10: Meta-atom design in visible frequency and theoretical result of our proposed meta-device

Our proposed design can be easily realized in visible light. We design a meta-atom at 633 nm as shown in Fig. S11. Based on these meta-atoms, we can achieve adaptively corrected planar scanning (similar functionality in the first device in the main text), the theoretical results are shown in Fig. S12. We believe that such samples can be fabricated using electron beam lithography.

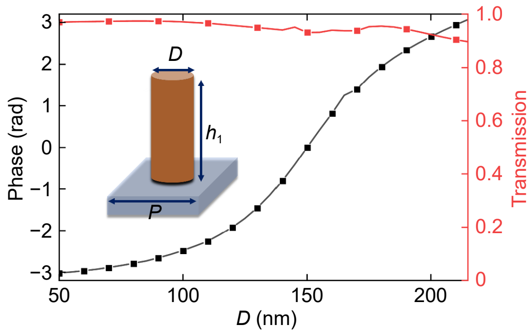

Fig. S11 | The transmission coefficient and phase of meta-atoms in the visible frequency range.

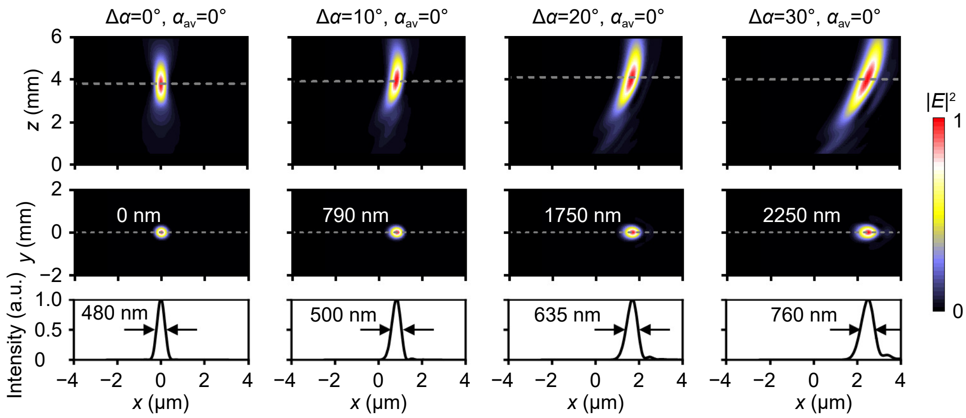

Fig. S12 | The theoretical result of meta-device for adaptively corrected planar scanning in visible frequency.

Section 11: Focal intensity control during scanning process

Here, we selected three cases corresponding to different parameters to demonstrate the capability of the focal intensity control in our design. Based on Eq. (6) in the main text, we can control the changes in the ratio of the working area during scanning by selecting appropriate parameters to break the dependence that the focal intensity decreases with the scanning angle increasing. As the rotation angle changes, the total phase distribution and working area ratio are shown in Fig. S13. The focal intensity of the meta-device for adaptively corrected planar scanning with different parameters corresponding to different scanning angles are shown in Fig. S14. Such intensity manipulation enables us to enhance our capacity for dynamic focal point control, which may be used to compensate for the typical decrease in intensity during scanning process or for other purposes.

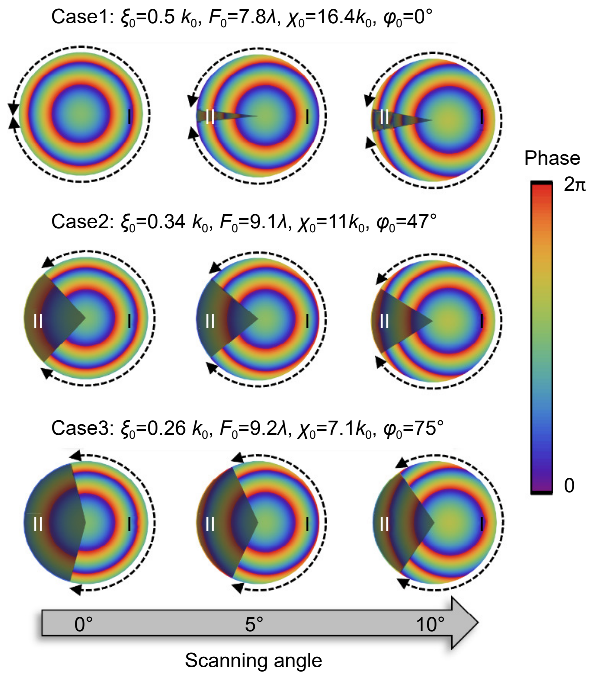

Fig. S13 | The working region and residual region of the meta-device for adaptively corrected planar scanning with different parameters corresponding to different scanning angles (0°,5°,10°).

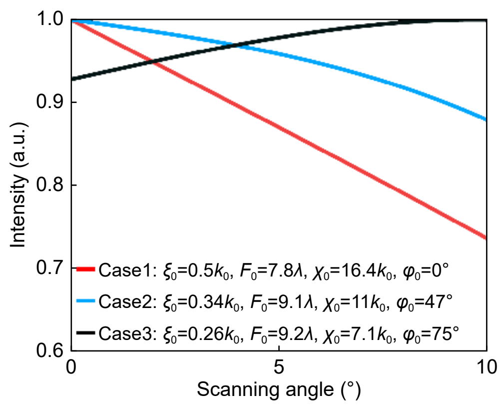

Fig. S14 | The focal intensity of the meta-device for adaptively corrected planar scanning with different parameters corresponding to different scanning angles (0°,5°,10°).

Section 12: The design of self-corrected dual-focal scanner

Based on the design concept of checkerboard pattern, we firstly reduce the parameter spaces $\boldsymbol{M}_A=\left\{\xi_{0,A},F_{0,A},\chi_{0,A},\varphi_{i,A}\right\}$ and $\boldsymbol{M}_B=\left\{\xi_{0,B},F_{0,B},\chi_{0,B},\varphi_{i,B}\right\}$. For the parameters within these two parameter spaces ($\boldsymbol{M}_A$ and $\boldsymbol{M}_B$), respectively, they need to satisfy $\chi_{0,A}=\chi_{0,B}$, $\left|\xi_{1,A}\right|=\left|\xi_{2,A}\right|=0.5k_0$, $\left|\xi_{1,B}\right|=\left|\xi_{2,B}\right|=0.5k_0$. In this case, as the first layer ($i=1$) is composed of subsection A and subsection B, this makes the parameters also need to satisfy: $\xi_{1,A}=\xi_{1,B}$, $F_{0,A}=F_{0,B}$, $\varphi_{1,A}=\varphi_{1,B}$ and $\chi_{1,A}=\chi_{1,B}$. At last, we set $\xi_{1,A}=\xi_{2,A}=\xi_{1,B}=0.5k_0\widehat{v}_i$ and $\xi_{2,B}=0.5k_0S(-2\gamma)\widehat{v}_i$, where $S(-2\gamma)=\begin{pmatrix}\cos(-2\gamma) & \sin(-2\gamma)\\ -\sin(-2\gamma) & \cos(-2\gamma)\end{pmatrix}$ and $\gamma=30°$ is taken to minimize the interaction of the two foci. Thus the parameter spaces $\boldsymbol{M}_A$ and $\boldsymbol{M}_B$ are reduced as $\boldsymbol{M}'_A=\left\{F_0,\chi_0,\Delta\varphi_{0,A}\right\}$ and $\boldsymbol{M}'_B=\left\{F_0,\chi_0,\Delta\varphi_{0,B}\right\}$, where $F_{0,A}=F_{0,B}=F_0$, $\Delta\varphi_{0,A}=\left(\varphi_{2,A}-\varphi_{1,A}\right)/2$, $\Delta\varphi_{0,B}=\left(\varphi_{2,B}-\varphi_{1,B}\right)/2$, $\chi_{1,A}=\chi_{2,A}=\chi_{1,B}=\chi_{2,B}=\chi_0$.

Based on the reduced parameter spaces, we obtain the position of the two foci respectively as a function of the rotation angle of metasurface:

1) For the focus A,

$$\begin{cases}\chi_A(\Delta\alpha,\alpha_{\mathrm{av}})=\sin(\Delta\alpha)\cos(\alpha_{\mathrm{av}})R(\Delta\alpha)\\ y_A(\Delta\alpha,\alpha_{\mathrm{av}})=\sin(\Delta\alpha)\sin(\alpha_{\mathrm{av}})R(\Delta\alpha)\\ z_A(\Delta\alpha)=\cos(\Delta\alpha)R(\Delta\alpha)\end{cases},\tag{S14}$$

where $\Delta\alpha$, α_{av}, $R(\Delta\alpha)$ are defined in Eq. (4) in the main text.

2) For the focus B,

$$\begin{cases}\chi_B(\Delta\alpha,\alpha_{\mathrm{av}})=\sin(\Delta\alpha-\gamma)\cos(\alpha_{\mathrm{av}}-\gamma)R(\Delta\alpha-\gamma)\\ y_B(\Delta\alpha,\alpha_{\mathrm{av}})=\sin(\Delta\alpha-\gamma)\sin(\alpha_{\mathrm{av}}-\gamma)R(\Delta\alpha-\gamma)\\ z_B(\Delta\alpha)=\cos(\Delta\alpha-\gamma)R(\Delta\alpha-\gamma)\end{cases},\tag{S15}$$

where γ can affect the position of the focus B.

With Eq. (S14) and Eq. (S15), we define the following Figureures of merit to find the optimal parameters in the reduced parameter spaces to achieve the desired functionality, respectively.

1) For the focus A,

$$\begin{cases}\bar{\eta}_A=1-\dfrac{1}{\pi}\dfrac{\int_0^{\Delta\alpha_{\max}}\left(\left|\Delta\alpha-\Delta\varphi_{0,A}\right|\right)\mathrm{d}\Delta\alpha}{\Delta\alpha_{\max}}\\ \bar{\Delta}_A=\dfrac{\int_0^{\Delta\alpha_{\max}}\sqrt{\left(z_A(\Delta\alpha)-h_A\right)^2}\mathrm{d}\Delta\alpha}{\Delta\alpha_{\max}}\end{cases},\tag{S16}$$

where h_A is defined in Eq. (9) in the main text.

2) For the focus B,

$$\begin{cases}\bar{\eta}_B=1-\dfrac{1}{\pi}\dfrac{\int_0^{\Delta\alpha_{\max}}\left(\left|\Delta\alpha-\Delta\varphi_{0,B}\right|\right)\mathrm{d}\Delta\alpha}{\Delta\alpha_{\max}}\\ \bar{\Delta}_B=\dfrac{\int_0^{\Delta\alpha_{\max}}\sqrt{\left(z_B(\Delta\alpha)+l_B\sqrt{x_B^2(\Delta\alpha,\alpha_{\mathrm{av}})+y_B^2(\Delta\alpha,\alpha_{\mathrm{av}})}-h_B\right)^2}\mathrm{d}\Delta\alpha}{\Delta\alpha_{\max}}\end{cases},\tag{S17}$$

where l_B and h_B are defined in Eq. (9) in the main text.

Figure S15 shows the optimal parameters finding results. In this case, the positive and negative of the maximum scanning angle represents the direction of increasing transverse shift along the focal point and decreasing transverse position along the focal point, respectively. The stars indicate the optimal parameters for the desired results: $F_0 = 8.4\lambda$, $\chi_0 = 16.3k_0$, $\Delta\varphi_{0,A} = 15°$, $\Delta\varphi_{0,B} = -15°$.

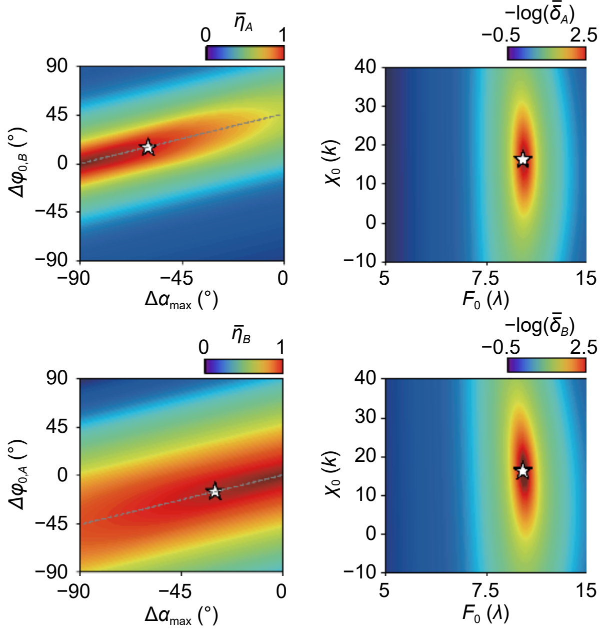

Fig. S15 | Optimal parameters searching process of focus *A* (**a**) and *B* (**b**).

Figure S16 shows the theoretical and simulated electric field distributions on two vertical planes for two focal spots, with azimuthal angle 0° and 30°, and two horizontal planes at focal planes, respectively. As the rotation angle $\Delta\alpha$ increase, the simulated focal positions precisely matched the theoretical predictions.

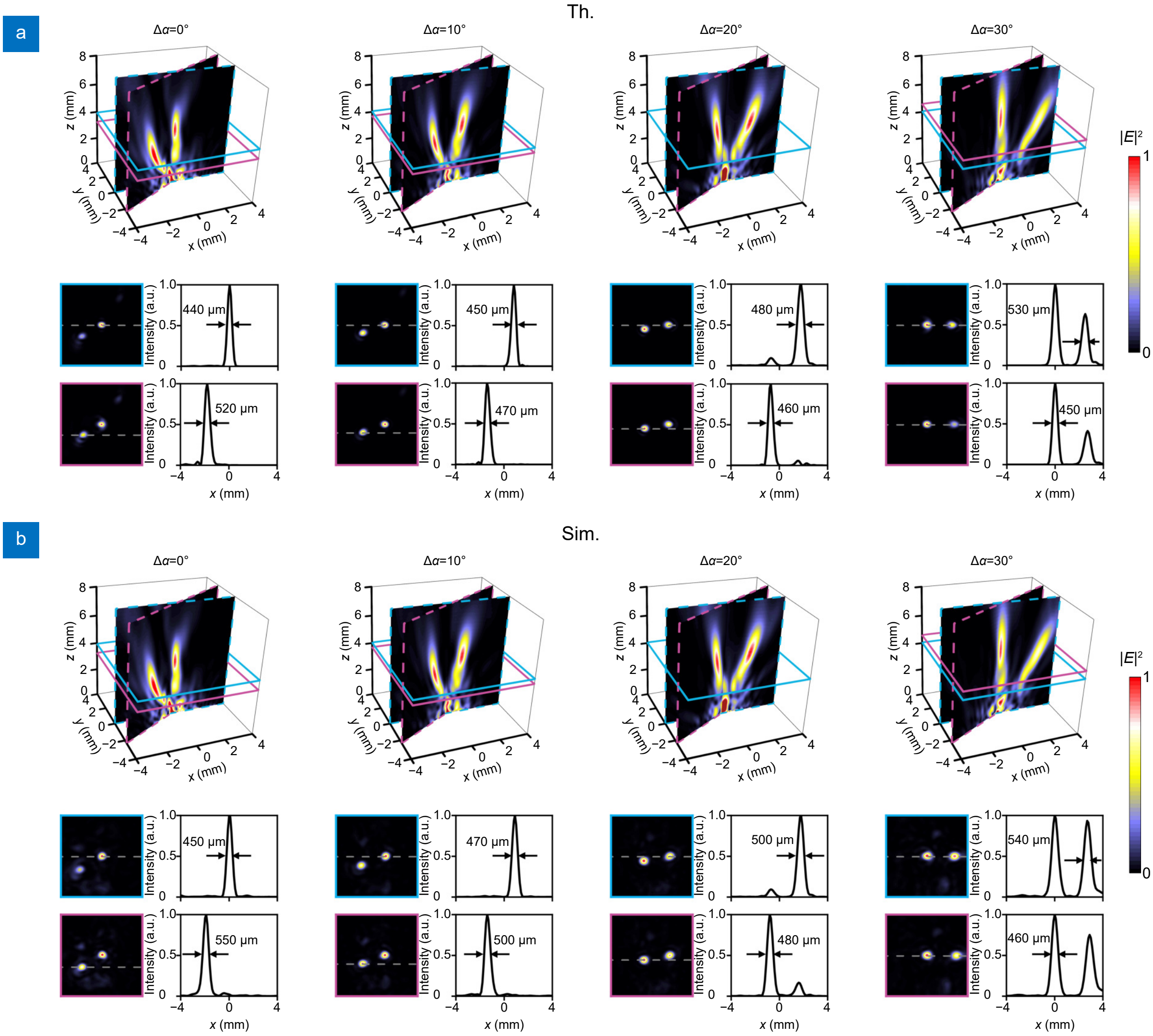

Fig. S16 | Terahertz characteristics of the adaptively corrected dual-focus scanner. (**a**) Theoretical and (**b**) simulated intensity distributions on two vertical planes (top) for two focal spots at the azimuthal angle 0° (dashed blue) and 30° (dashed pink) corresponding to different $\Delta\alpha$, with two horizontal planes (bottom left) at focal plane for focal spot *A* (solid blue) and *B* (solid pink). The intensity profiles along the diameter (bottom right) at the focal plane with the FWHM marked.